Anomalous Hall effect in noncollinear antiferromagnetic Mn_3NiN thin films

David Boldrin,[1,*] Ilias Samathrakis,[2] Jan Zemen,[3] Andrei Mihai,[4] Bin Zou,[4] Freya Johnson,[1] Bryan D. Esser,[5,6] David W. McComb,[5,6] Peter K. Petrov,[4] Hongbin Zhang,[2] and Lesley F. Cohen[1]

[1]*Department of Physics, Blackett Laboratory, Imperial College London, London SW7 2AZ, United Kingdom*
[2]*Institute of Materials Science, TU Darmstadt, 64287, Darmstadt, Germany*
[3]*Faculty of Electrical Engineering, Czech Technical University in Prague, Technická 2, Prague 166 27, Czech Republic*
[4]*Department of Materials, Imperial College London, London SW7 2AZ, United Kingdom*
[5]*Center for Electron Microscopy and Analysis, The Ohio State University, Columbus, Ohio 43212, USA*
[6]*Department of Materials Science and Engineering, The Ohio State University, Columbus, Ohio 43210, USA*

(Received 15 February 2019; published 23 September 2019)

We have studied the anomalous Hall effect (AHE) in strained thin films of the frustrated antiferromagnet Mn_3NiN. The AHE does not follow the conventional relationships with magnetization or longitudinal conductivity and is enhanced relative to that expected from the magnetization in the antiferromagnetic state below $T_N = 260$ K. This enhancement is consistent with origins from the noncollinear antiferromagnetic structure, as the latter is closely related to that found in Mn_3Ir and Mn_3Pt where a large AHE is induced by the Berry curvature. As the Berry-phase-induced AHE should scale with spin-orbit coupling, yet larger AHE may be found in other members of the chemically flexible Mn_3AN structure.

DOI: 10.1103/PhysRevMaterials.3.094409

I. INTRODUCTION

The realization of large anomalous Hall effects (AHE) in antiferromagnets is of significant importance from both a fundamental and practical perspective [1]. Conventionally, the AHE is considered proportional to magnetization and so large effects are not anticipated in antiferromagnets. However, over the past decade it has been appreciated that a spontaneous AHE can arise in antiferromagnets with zero net magnetization that break certain symmetries, usually via the inclusion of spin-orbit coupling (SOC) [2–5]. In addition to SOC a lack of inversion symmetry is also required, such as found in noncollinear antiferromagnetic (AFM) structures that arise from geometric frustration. In such scenarios, large values of the Berry curvature can be obtained and, consequently, a large intrinsic AHE. From a fundamental perspective, the AHE in antiferromagnets is of interest as the underlying physics also give rise to exotic quasiparticle excitations, such as the recently observed Dirac and Weyl fermions [6,7]. From a technological perspective, the AHE offers novel opportunities in spintronics devices that utilize control of the AFM state despite zero magnetization [8,9].

Mn antiperovskites, with general formula Mn_3AN, have attracted a revival of interest due to a range of fascinating phenomena, such as temperature-independent resistivity [10], abnormal thermal expansion [11], and barocaloric effects [12,13]. These properties are underpinned by a noncollinear AFM structure and magnetovolume coupling that induces strong first-order character to the magnetic transitions. Moreover, the chemical flexibility of the structure allows many elements to be doped on the A site, providing synthetic control of their functional properties [11]. In thin-film form the family are predicted to host giant piezomagnetism, a linear dependence of the magnetization on the elastic stress tensor [14,15], a characteristic we have recently demonstrated experimentally in Mn_3NiN thin films [16]. Taken together, these materials offer a unique mixture of magnetic and structural properties and yet the magnetoconductance is a property that is little examined [17], particularly as a function of strain.

We consider the A = Ni member of the family, Mn_3NiN, studied previously in the bulk for its temperature-independent electrical resistivity [10], above its strongly first-order paramagnetic-to-AFM transition at $T_N = 260$ K, where the material undergoes a 0.4% volume change. In the AFM phase, the moments which reside on the Mn sites undergo a temperature-dependent rotation between two high-symmetry structures on cooling, termed Γ^{5g} and Γ^{4g} [see Figs. 1(a) and 1(b), respectively], both closely related to the magnetic structure found in the binary alloys Mn_3A [18,19]. In this article, we first calculate the intrinsic anomalous Hall conductivity (AHC) in Mn_3NiN and show that a large AHC is expected when the material adopts the Γ^{4g} noncollinear AFM structure, consistent with the symmetry analysis [17,20,21], due to a large Berry-phase contribution. Moreover, we show that the AHC is highly sensitive to strain. Experimentally, we measure the AHE in Mn_3NiN thin films and show that it increases considerably below T_N despite negligible change in the magnitude of the magnetization. We attribute the large AHE in the AFM state below T_N to the noncollinear Γ^{4g} magnetic structure. The enlarged AHE in AFM Mn_3NiN thin films, combined with its calculated sensitivity to strain, opens the possibility for significant piezospintronic effects in this material as well as the wider Mn_3AN family.

*Corresponding author: d.boldrin@imperial.ac.uk

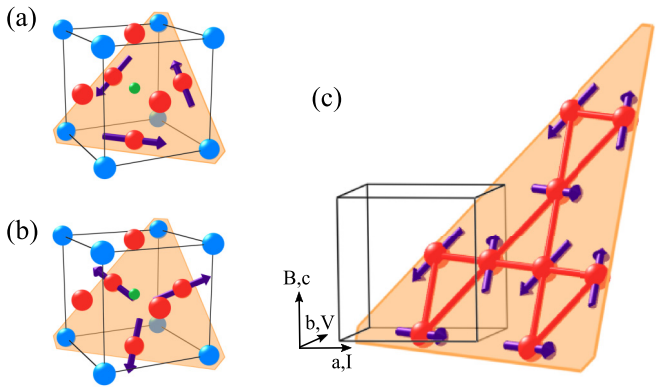

FIG. 1. [(a) and (b)] The noncollinear AFM structures termed Γ^{5g} and Γ^{4g}, respectively. (c) The orientation of the kagome (111) plane relative to the cubic unit cell. The substrate is in the (110) plane. For magnetotransport, voltage and current axes are in the (110) plane, with the magnetic field applied along [001].

II. CALCULATION OF THE ANOMALOUS HALL EFFECT IN Mn_3NiN

We begin with calculations of the anomalous Hall conductivity in Mn_3NiN, and the Berry-phase contribution to it, performed as a function of lattice strain. The projector augmented wave method as implemented in the VASP code [22] was used, where the exchange correlation functional is formulated in the generalized gradient approximation as parameterized by Perdew-Burke-Ernzerhof [23]. Our results were obtained using a $13 \times 13 \times 13$ Γ-centered k-mesh sampling and a 500-eV energy cut-off to guarantee good convergence. The valence configurations of Mn, Ni, and N, are $3d^6 4s^1$, $3d^8 4s^2$, and $2s^2 2p^3$, respectively. The scheme in Ref. [24] was followed so as to project the obtained density functional theory (DFT) Bloch wave functions onto maximally localized Wannier functions (MLWF). The MLWF [24], which were constructed for the s, p, and d orbitals of the Mn and Ni atoms, and the s and p orbitals for N were generated on an $8 \times 8 \times 8$ k-mesh. The intrinsic anomalous Hall conductivity is evaluated by integrating the Berry curvature using Wanniertools [25] on a $500 \times 500 \times 500$ k-mesh, according to the formula [26]:

$$\sigma_{\alpha,\beta} = \frac{-e^2}{\hbar} \int \frac{dk}{(2\pi^3)} \sum_{n(\text{occ.})} f[\epsilon(k) - \mu] \Omega_{n,\alpha,\beta}(k), \quad (1)$$

$$\Omega_{n,\alpha,\beta}(k) = -2I \sum_{m \neq n} \frac{\langle km|v_\alpha(k)|kn\rangle \langle kn|v_\beta(k)|km\rangle}{[\epsilon_{kn} - \epsilon_{km}]^2}, \quad (2)$$

where $f[\epsilon(k) - \mu]$ denotes the Fermi distribution function with Fermi energy indicated by μ and ϵ_{kn} (ϵ_{km}) are the energy eigenvalues corresponding to occupied (unoccupied) Bloch band n (m), where $v_\alpha(k)$ [$v_\beta(k)$] corresponds to the velocity operator in Cartesian coordinates.

The calculated AHC in Mn_3NiN as a function of strain is shown in Fig. 2(a). It is clear that compressive (tensile) strain enhances (reduces) the intrinsic AHC, as obtained by DFT calculations assuming the Γ^{4g} magnetic structure. It is noted that the unstrained Γ^{5g} state is invariant under the application of $M_{\bar{1}10}$ and equivalent mirror planes. Preservation of such

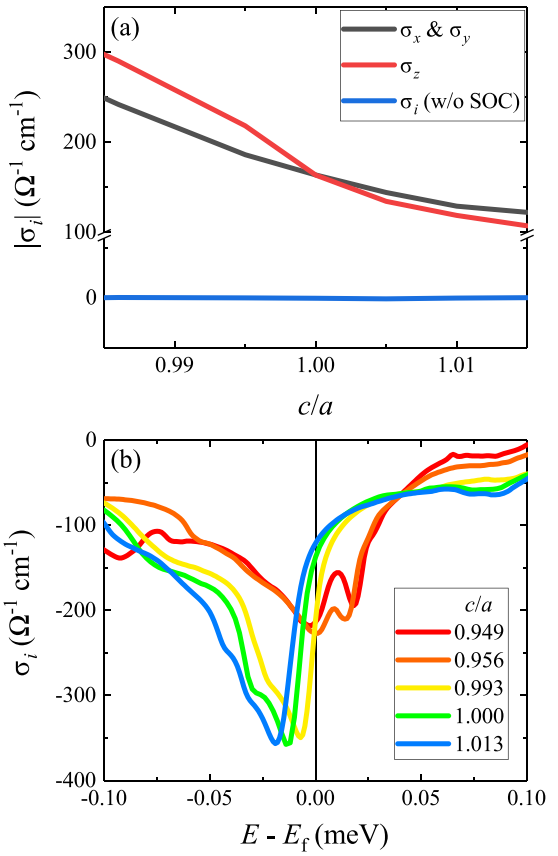

FIG. 2. (a) The behavior of the calculated intrinsic anomalous Hall conductivity components, σ_i, under strain. (b) The AHC for different strain values as a function of energy.

symmetry operations makes the Berry curvature vanish after integrating over the whole Brillouin zone [17]. Hence, all AHC components are zero. When finite strain is applied the symmetry is reduced to space group $C2/m$ (12.58), forcing only σ_z to be zero (see Fig. S1 [27]). However, the unstrained Γ^{4g} state is invariant under the application of the combined $TM_{\bar{1}10}$ and equivalent symmetry operations. In this case, the Berry curvature is an even function of the k vector which leads to finite AHC values after integration over the Brillouin zone [17,20]. In the strained case, the symmetry operations impose $\sigma_x = \sigma_y \neq 0$ and $\sigma_z \neq 0$. The form of the AHC tensor for both strained configurations was constructed using Refs. [28,29] and is presented in Table I. Similar behavior of the AHC is predicted for unstrained Mn_3GaN [17,21]. Figure 2(b) shows how the AHC changes as the system moves away from the

TABLE I. Symmetry-imposed AHC tensor for the canted Γ^{4g} and Γ^{5g} states under strain. The two-index and single-index AHC notations are related by $\sigma_{xy} = \sigma_z$, $\sigma_{zx} = \sigma_y$, and $\sigma_{yz} = \sigma_x$.

Magnetic phase	Canted Γ^{4g}	Canted Γ^{5g}
Magnetic Space Group	$C2'/m'$ (12.62)	$C2/m$ (12.58)
AHC tensor	$\begin{bmatrix} 0 & \sigma_{xy} & -\sigma_{zx} \\ -\sigma_{xy} & 0 & \sigma_{zx} \\ \sigma_{zx} & -\sigma_{zx} & 0 \end{bmatrix}$	$\begin{bmatrix} 0 & 0 & -\sigma_{zx} \\ 0 & 0 & -\sigma_{zx} \\ \sigma_{zx} & \sigma_{zx} & 0 \end{bmatrix}$

Fermi energy for different strain values. A shift of the Fermi energy by only 0.05 eV can lead to a change of 150 S cm^{-1} in the calculated conductivity value, meaning that the measured AHC value will be sensitive to a number of experimental factors, e.g. electronic doping. Interestingly, as the anomalous Nernst effect is related to the derivative of AHC with respect to the Fermi energy, Fig. 2(b) suggests it should be significant in these materials, with the anomalous Nernst coefficient reaching $-22822\,\mathrm{S\,cm^{-1}eV^{-1}}$ for $c/a = 0.993$, an order of magnitude larger than Mn_3Sn [30].

The intrinsic contribution shown here relies on the finite spin-orbit coupling interaction in Mn_3NiN. The AHC is vanishingly small if the spin-orbit coupling is set to zero. This can be understood when considering that the magnetic moments of all atoms form a coplanar spin configuration and the R_ST symmetry is preserved in the absence of spin-orbit coupling [20]. This is indeed observed in our explicit calculations on both Γ^{5g} and Γ^{4g} configurations [see Fig. 2(a)]. That is, we find that the topological Hall contribution in the coplanar spin geometry is insignificant. Furthermore, we suspect that there would be no net contribution to the AHC due to the Weyl points [3]. This is due to the fact that the Weyl points always appear in pairs with opposite chiralities and for magnetic materials they are supposed to be at the same energy [31].

III. MAGNETOMETRY AND MAGNETOTRANSPORT MEASUREMENTS

We now turn to experimental results on our Mn_3NiN thin films, which were grown as described in Reference [16]. The sample primarily examined in this study is a 50-nm-thick Mn_3NiN film on a (001) $(LaAlO_3)_{0.3}(Sr_2TaAlO_6)_{0.7}$ (LSAT) substrate ($a_{\mathrm{LSAT}} = 3.868$ Å) and to check consistency we also measure a 100-nm film on the same substrate. Energy-dispersive x-ray spectroscopy (EDX) found the Mn:Ni ratios for the 50- and 100-nm films to be 3:0.96(8) and 3:0.99(4). Considering the similar lattice parameters of Mn_3NiN ($a_{\mathrm{bulk}} = 3.8805$ Å [16]) and LSAT, precise determination of the strain is challenging. x-Ray diffraction (XRD) data collected on the (002) reflection on the 50- and 100-nm Mn_3NiN films grown on LSAT are shown in Fig. 3(a) along with a high-angle annular dark-field scanning transmission electron microscopy (HAADF-STEM) image taken of the 50-nm film. The HAADF-STEM shows a highly crystalline film with a slight rotation around the [010] direction relative to the substrate, meaning the lattice parameters cannot be obtained from this image. However, we have previously shown that film growth is unusual as substrates with larger (smaller) lattice parameter produce in-plane compressive (tensile) strained films [16]. The out-of-plane XRD of the (002) reflection shows that the film peaks cannot be resolved from the substrate and therefore $c = 3.868(3)$ Å. The (200) and (100) reflections of the 50- and 100-nm films are shown in Fig. 3(b), both of which clearly show a further peak at larger d spacing compared to the out-of-plane data. Fitting the (100) peak gives a lattice parameter of 3.876(1) Å and 3.8787(3) Å for the 100- and 50-nm films, respectively, giving $c/a = 0.998(1)$ and 0.997(1) and biaxial strain of $\epsilon_{xx} = 0.09(4)\%$ and $0.12(4)\%$. Thus, these results confirm that these samples are under tensile strain in the plane of the film.

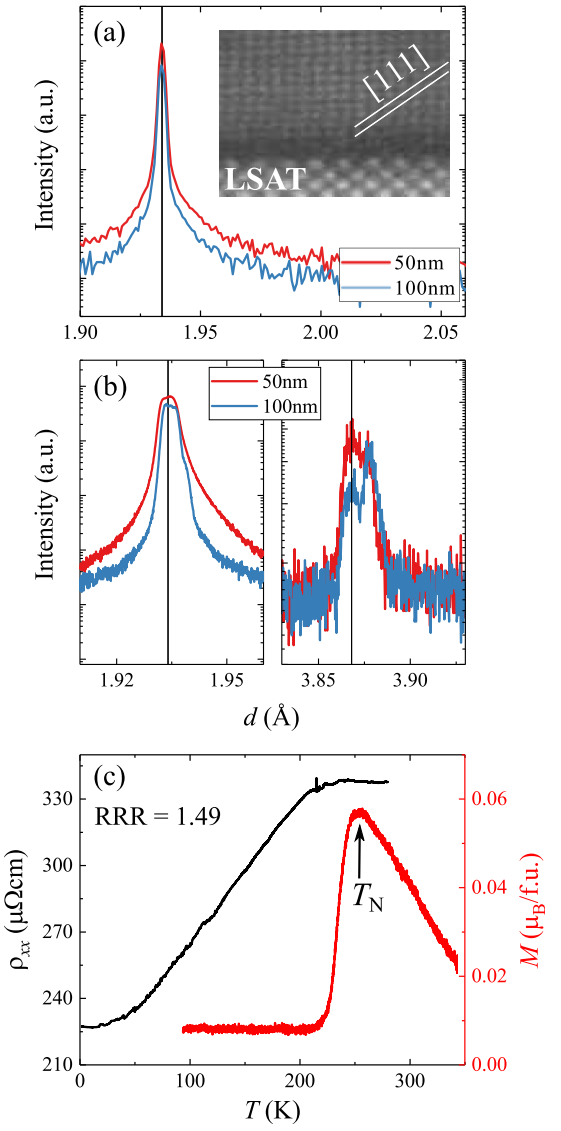

FIG. 3. (a) Out-of-plane x-ray diffraction data of the (002) reflection for both the 50- and 100-nm Mn_3NiN films and a HAADF-STEM image (full scale 3.75 nm) of the 50-nm film; (b) $h00$ grazing incidence XRD scans of the $h = 1$ and 2 reflections measured on the 50- and 100-nm films. In both (a) and (b) the vertical black line indicates the position of the substrate peak. (c) Longitudinal resistivity (left axis) and magnetization (right axis) measured out of plane as a function of temperature on the 50-nm film. The Neél temperature T_N and the residual resistance ratio (RRR) are indicated.

Four terminal magnetotransport measurements were performed as a function of temperature using the standard van der Paauw method. The temperature-dependent longitudinal resistivity, ρ_{xx}, is shown in Fig. 3(c) along with the temperature-dependent magnetization performed using the VSM option of a Quantum Design Physical Property Measurement System (PPMS-9T). The residual resistance ratio of 1.5 is in line with structurally similar films [32]. The film shows a transition to an AFM state at $T_N = 250$ K.

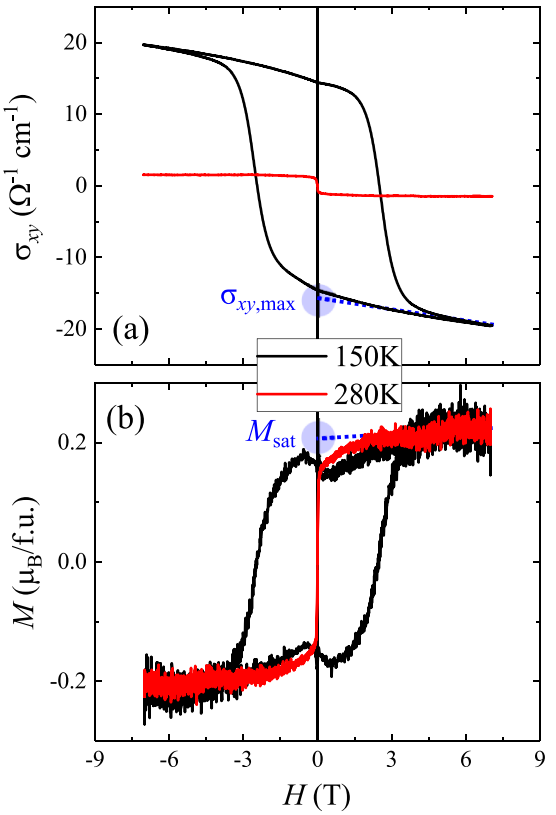

FIG. 4. (a) Hall conductivity and (b) out-of-plane magnetization measured as a function of field above and below T_N of the 50-nm Mn_3NiN (LSAT) film.

Magnetotransport measurements were performed at different temperatures above and below T_N. Regarding the measurement geometry, it is important to note that the kagome (111) plane that the moments reside in lies at ∼45° to the film surface normal, as shown in Fig. 1(c). In the Mn_3A materials, the maximum AHE is observed when the applied field is in the kagome plane, and both voltage and current are orthogonal to this [5]. In our thin films, we are unable to access this geometry. Instead, the applied field is applied normal to the film surface along c, with voltage and current directions both orthogonal to this axis and each other.

The Hall conductivity, σ_{xy}, is commonly defined as $\sigma_{xy} = -\rho_{xy}/\rho_{xx}^2$ in the small-Hall-angle regime, $\rho_{xy} \ll \rho_{xx}$, which in our case ρ_{xy}/ρ_{xx} is smaller than 0.007 at all temperatures. Plots of $\sigma_{xy}(H)$ at different temperatures for the 50-nm film on LSAT are shown in Fig. 4(a) and can be compared directly with magnetization measurements (out of plane) in the same field region in Fig. 4(b). The shape of both Hall conductivity and magnetization are closely matched in the region shown above and below T_N. However, it is clear that the magnitude of σ_{xy} is quite different above and below T_N, whereas the magnitude of the magnetization remains roughly constant.

Conventionally, measurements of transverse resistivity have contributions from the normal Hall effect proportional to the applied field, R_0H, and a term proportional to the magnetization, R_SM. As discussed, a further intrinsic term can contribute in case of an electronic band structure with a large Berry curvature. Deconvoluting these effects can

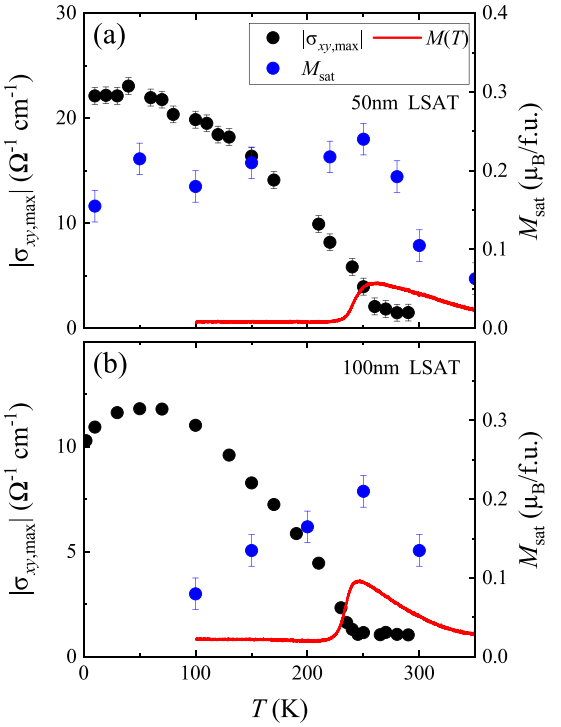

FIG. 5. Spontaneous Hall conductivity (left axis), saturation magnetization, M_{sat} (right axis), and zero-field-cooled magnetization in $H = 0.05$ T (right axis) measured on (a) the 50-nm and (b) the 100-nm LSAT film.

be performed by observing their temperature dependencies [6,33]. In Fig. 5(a) we compare directly the temperature dependence of the Hall conductivity, $|\sigma_{xy}|$ [where the normal Hall contribution has been removed, see Fig. 4(a)], and the saturation magnetization, M_{sat}, for the 50-nm LSAT film. For a simple collinear ferromagnet one would expect σ_{xy} to scale with the magnetization. This relationship approximately

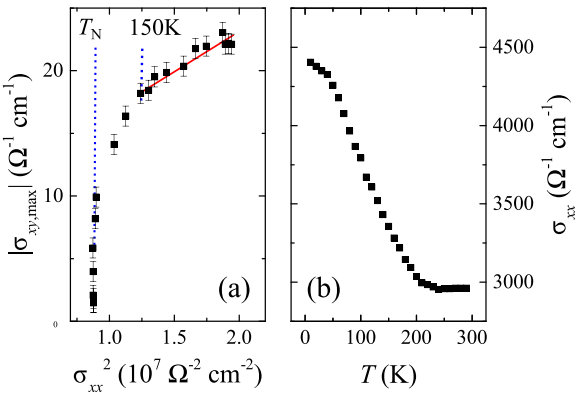

FIG. 6. (a) A plot of the Hall conductivity, $|\sigma_{xy}|$, as a function of the longitudinal conductivity, σ_{xx}^2, and (b) the longitudinal resistivity, σ_{xx}, as a function of temperature. The vertical blue lines in (a) indicate two distinct regions: (i) between T_N and $T = 150$ K, where σ_{xx} remains relatively constant, and (ii) below $T = 150$ K, where an upturn in σ_{xx} is observed. The latter region has a roughly linear dependence between $|\sigma_{xy}|$ and σ_{xx}^2, indicated by the red line guiding the eye.

TABLE II. A comparison of the anomalous Hall effects present in a variety of magnetic materials. The final column parameterizes the strength of the AHE relative to the magnetization of the material.

Sample	T (K)	M_{sat} (μ_B ion^{-1})	$\lvert\sigma_{xy}\rvert$ (Ω^{-1} cm^{-1})	σ_{xx} (Ω^{-1} cm^{-1})	$\lvert\sigma_{xy}\rvert$ per M (Ω^{-1} cm^{-1} μ_B^{-1} ion)
Mn_3NiN (LSAT 50 nm)	10	0.053	22	4100	415
Mn_3NiN (LSAT 50 nm)	300	0.033	1.5	3000	35
Mn_3Sn [5]	100	0.003	100	3125	40 000
Mn_3Pt [9]	100	0.005	100	3300	20 000
Fe_3Sn_2 [6]	300	1.7	180	2000	105
Mn_3CuN [32]	5	0.23	4.2	2630	18
Fe (2.5 nm) [35]	300	2.2	300	20000	135
$Co_3Sn_2S_2$ [36]	100	0.25	1000	7000	4000

holds between 300 K and 250 K, where the magnetization increases linearly and the small but finite $|\sigma_{xy}|$ behaves similarly. However, below T_N, $|\sigma_{xy}|$ increases steadily and does not saturate until $T \sim 50$ K, whereas the magnetization peaks at T_N and remains roughly constant on further cooling. To check the reproducibility of this result, we performed equivalent measurements on a 100-nm-thick film grown on LSAT shown in Fig. 5(b). For the 100-nm film on LSAT, $|\sigma_{xy}|$ shows a remarkably similar temperature dependence, although saturates at roughly half the value of the 50-nm film at 10 K. Given the larger strain expected in the 50-nm film from the in-plane lattice parameter, the $|\sigma_{xy}|$ values of the two films agrees with the strain-related trend shown in Fig. 2(a). Taken together, the behavior below T_N of either film cannot be reconciled with the conventional description of the AHE being proportional to magnetization.

Further understanding of the origins of the Hall conductivity can be gained through comparison with the longitudinal conductivity [6,33]. Extrinsic contributions to the AHE are caused by scattering processes, which have similar temperature dependencies to the longitudinal conductivity. Thus, the scaling of both, in the absence of changes to magnetization, is given by the relationship [33,34]:

$$\sigma_{xy} = f(\sigma_{xx,0})\sigma_{xx}^2 + \sigma_{xy}^{\text{int}}, \tag{3}$$

where $\sigma_{xx,0}$ is the residual conductivity and σ_{xy}^{int} is the intrinsic anomalous Hall conductivity. A plot of $|\sigma_{xy}|$ against σ_{xx}^2 is shown in Fig. 6(a) for the 50-nm film on LSAT and the temperature dependence of σ_{xx} is in Fig. 6(b). While the relatively small residual resistance ratio of our film does not allow access to a large range of σ_{xx} values as a function of temperature, certain trends can be seen in the data. First, between T_N and ~150 K, where both the magnetization and longitudinal conductivity remain relatively constant (the latter changing by <10%), $|\sigma_{xy}|$ changes by an order of magnitude in a nonlinear relationship with σ_{xx}^2. Second, below 150 K, σ_{xx} begins to increase more rapidly, changing by ~40% by 10 K, while $|\sigma_{xy}|$ begins to plateau. In this region, $|\sigma_{xy}|$ has a much more linear dependence with σ_{xx}^2. This suggests the region has a contribution from extrinsic scattering-type processes, which is expected at low temperatures due to the increased carrier lifetime with larger σ_{xx}. In the high-temperature regime, the nonlinear dependence of $|\sigma_{xy}|$ with σ_{xx}^2 is not consistent with extrinsic scattering processes. Thus, we conclude that this behavior of $|\sigma_{xy}|$ in this regime cannot be accounted for by either extrinsic scattering processes or changes in magnetization.

In Table II we summarize the magnitude of the AHE in Mn_3NiN and compare to a number of other magnetic materials. First, we see that σ_{xy} is an order of magnitude larger in the AFM state than above T_N despite only a doubling of the size of M. Compared to an Fe thin film, the relative strength of the AHE to M in Mn_3NiN is around triple, further evidence that it is larger than expected. In antiperovskite Mn_3CuN, where the magnetic structure is a ferrimagnet, the AHE is roughly 5 times smaller than for A = Ni, and relative to its magnetization it is an order of magnitude smaller. In the purely AFM Mn_3A materials σ_{xy} is 5 times larger, while in the ferromagnetic Fe_3Sn_2 [6,37] and $Co_3Sn_2S_2$ [36] σ_{xy} is 9 and 50 times larger, respectively; all these examples have large SOC from Sn or Pt, which in turn increases the Berry curvature–driven AHE. The Mn_3AN material family is chemically flexible, with the A site taking many transition and post-transition metals, such that elements with large SOC may be incorporated. Therefore, our results should spur further experiments for an enlarged AHE with large SOC elements but also theoretical work to reveal the underlying physics giving rise to these effects.

IV. CONCLUSIONS

In conclusion, we have measured the AHE in strained thin films of Mn_3NiN and compared our results with theoretical predictions of the intrinsic effect for the Γ^{4g} AFM phase in addition to its strain dependence. We find a large Berry curvature induced by the noncollinear AFM structure which is of similar origin as that found in the isostructural Mn_3Pt. Theoretical analysis demonstrates that the intrinsic AHE is highly sensitive to strain, doping, and the ratio of Γ^{5g} and Γ^{4g}. Moreover, the AHE relies on spin-orbit coupling and therefore larger effects can be expected in the wider Mn_3AN family with heavier A elements. The predicted strain dependence of the AHE displays a sharp change in the AHC relative to the Fermi energy for compressively strained films, indicating that a large anomalous Nernst effect is expected in these materials. Recent papers demonstrating manipulation of AFM structures by growth on piezoelectric substrates [9] could inspire similar developments in Mn_3AN thin films where one could create large piezospintronic effects via strain coupling.

ACKNOWLEDGMENTS

We acknowledge support from the Henry Royce Institute made through EPSRC Grant No. EP/R00661X//1 and EPSRC Impact Acceleration Account funding: Localised magnetic repository (LoMaRe) a high-performance nonvolatile memory device. F.J. acknowledges funding through the EPSRC DTP Hitachi CASE award and LFC through The Leverhulme Trust grant ref RPG-2016-306. B.D.E. and D.W.M. acknowledge support from the Center for Emergent Materials at the Ohio State University, a National Science Foundation Materials Research Science and Engineering Center (Grant No. DMR-1420451). The work of J.Z. was supported by The Ministry of Education, Youth and Sports of the Czech Republic from the Large Infrastructures for Research, Experimental Development and Innovations project "IT4Innovations National Supercomputing Center LM2015070" and by the OP RDE program within the project International Mobility of Researchers MSCA-IF No. CZ.02.2.69/0.0/0.0/18_070/0010457. The authors acknowledge support from the DFG-SPP 1666 programme and the Lichtenberg high performance computer of TU Darmstadt. We thank Jakub Železný for fruitful discussions of the form of the AHC tensor and Joerg Wunderlich for useful discussions overall.

[1] N. Nagaosa, J. Sinova, S. Onoda, A. H. MacDonald, and N. P. Ong, Rev. Mod. Phys. **82**, 1539 (2010).

[2] H. Chen, Q. Niu, and A. H. MacDonald, Phys. Rev. Lett. **112**, 017205 (2014).

[3] J. Kübler and C. Felser, Europhys. Lett. **108**, 67001 (2014).

[4] Y. Zhang, Y. Sun, H. Yang, J. Železný, S. P. P. Parkin, C. Felser, and B. Yan, Phys. Rev. B **95**, 075128 (2017).

[5] S. Nakatsuji, N. Kiyohara, and T. Higo, Nature **527**, 212 (2015).

[6] L. Ye, M. Kang, J. Liu, F. V. Cube, C. R. Wicker, T. Suzuki, C. Jozwiak, A. Bostwick, E. Rotenberg, D. C. Bell, L. Fu, R. Comin, and J. G. Checkelsky, Nature **555**, 638 (2018).

[7] K. Kuroda, T. Tomita, M. T. Suzuki, C. Bareille, A. A. Nugroho, P. Goswami, M. Ochi, M. Ikhlas, M. Nakayama, S. Akebi, R. Noguchi, R. Ishii, N. Inami, K. Ono, H. Kumigashira, A. Varykhalov, T. Muro, T. Koretsune, R. Arita, S. Shin, T. Kondo, and S. Nakatsuji, Nat. Mater. **16**, 1090 (2017).

[8] L. Šmejkal, Y. Mokrousov, B. Yan, and A. H. MacDonald, Nat. Phys. **14**, 242 (2018).

[9] Z. Q. Liu, H. Chen, J. M. Wang, J. H. Liu, K. Wang, Z. X. Feng, H. Yan, X. R. Wang, C. B. Jiang, J. M. D. Coey, and A. H. MacDonald, Nat. Electron. **1**, 172 (2018).

[10] E. O. Chi, W. S. Kim, and N. H. Hur, Solid State Commun. **120**, 307 (2001).

[11] K. Takenaka, M. Ichigo, T. Hamada, A. Ozawa, T. Shibayama, T. Inagaki, and K. Asano, Sci. Technol. Adv. Mater. **15**, 015009 (2014).

[12] D. Matsunami, A. Fujita, K. Takenaka, and M. Kano, Nat. Mater. **14**, 73 (2014).

[13] D. Boldrin, E. Mendive-Tapia, J. Zemen, J. B. Staunton, T. Hansen, A. Aznar, J.-L. Tamarit, M. Barrio, P. Lloveras, J. Kim, X. Moya, and L. F. Cohen, Phys. Rev. X **8**, 041035 (2018).

[14] J. Zemen, Z. Gercsi, and K. G. Sandeman, Phys. Rev. B **96**, 024451 (2017).

[15] J. Zemen, E. Mendive-Tapia, Z. Gercsi, R. Banerjee, J. B. Staunton, and K. G. Sandeman, Phys. Rev. B **95**, 184438 (2017).

[16] D. Boldrin, A. P. Mihai, B. Zou, J. Zemen, R. Thompson, E. Ware, B. V. Neamtu, L. Ghivelder, B. Esser, D. W. McComb, P. Petrov, and L. F. Cohen, ACS Appl. Mater. Interfaces **10**, 18863 (2018).

[17] G. Gurung, D.-F. Shao, T. R. Paudel, and E. Y. Tsymbal, Phys. Rev. Materials **3**, 044409 (2019).

[18] K. Yasukochi, K. Kanematsu, and T. Ohoyama, J. Phys. Soc. Jpn. **16**, 1123 (1961).

[19] E. Krén, G. Kádár, L. Pál, E. Zsoldos, M. Barberon, and R. Fruchart, J. Phys. Colloq. **32**, C1-980 (1971).

[20] M. T. Suzuki, T. Koretsune, M. Ochi, and R. Arita, Phys. Rev. B **95**, 094406 (2017).

[21] I. Samathrakis and H. Zhang, arXiv:1905.11798 [cond-mat.mtrl-sci].

[22] G. Kresse and J. Hafner, Phys. Rev. B **47**, 558 (1993).

[23] J. P. Perdew, K. Burke, and M. Ernzerhof, Phys. Rev. Lett. **77**, 3865 (1996).

[24] A. A. Mostofi, J. R. Yates, Y. S. Lee, I. Souza, D. Vanderbilt, and N. Marzari, Comput. Phys. Commun. **178**, 685 (2008).

[25] Q. S. Wu, S. N. Zhang, H. F. Song, M. Troyer, and A. A. Soluyanov, Comput. Phys. Commun. **224**, 405 (2018).

[26] D. Xiao, M. C. Chang, and Q. Niu, Rev. Mod. Phys. **82**, 1959 (2010).

[27] See Supplemental Material at http://link.aps.org/supplemental/10.1103/PhysRevMaterials.3.094409 for the calculated intrinsic anomalous Hall conductivity under strain for the Γ_{5g} structure.

[28] J. Železný, https://bitbucket.org/zeleznyj/linear.

[29] L. Šmejkal and T. Jungwirth, arXiv:1804.05628 [cond-mat.mes-hall].

[30] G. Y. Guo and T. C. Wang, Phys. Rev. B **96**, 224415 (2017).

[31] G. B. Halász and L. Balents, Phys. Rev. B **85**, 035103 (2012).

[32] T. Matsumoto, T. Hatano, T. Urata, K. Iida, K. Takenaka, and H. Ikuta, Phys. Rev. B **96**, 205153 (2017).

[33] Y. Tian, L. Ye, and X. Jin, Phys. Rev. Lett. **103**, 087206 (2009).

[34] A. Shitade and N. Nagaosa, J. Phys. Soc. Jpn. **81**, 083704 (2012).

[35] S. Sangiao, L. Morellon, G. Simon, J. M. DeTeresa, J. A. Pardo, J. Arbiol, and M. R. Ibarra, Phys. Rev. B **79**, 014431 (2009).

[36] Q. Wang, Y. Xu, R. Lou, Z. Liu, M. Li, Y. Huang, D. Shen, H. Weng, S. Wang, and H. Lei, Nat. Commun. **9**, 3681 (2018).

[37] T. Kida, L. A. Fenner, A. A. Dee, I. Terasaki, M. Hagiwara, and A. S. Wills, J. Phys.: Condens. Matter **23**, 112205 (2011).